Heat treatment and properties of a hot work tool steel fabricated by additive manufacturing

Faraz Deirmina[a,b], Nicola Peghini[a], Bandar AlMangour[c], Dariusz Grzesiak[d], Massimo Pellizzari[a]*

[a] Department of Industrial Engineering, University of Trento, via Sommarive 9, 38123, Trento, Italy

[b] Powder R&D, SANDVIK ADDITIVE MANUFACTURING, Mossvägen 10, 811 82 Sandviken, Sweden

[c] Saudi Arabia Basic Industries Corporation, P. O. Box 11669, Jubail 31961, Saudi Arabia

[d] Department of Mechanical Engineering and Mechatronics, West Pomeranian University of Technology, Szczecin, Poland

* Corresponding author, Massimo.Pellizzari@unitn.it

Abstract

Additive manufacturing (AM) is increasingly used for the manufacturing of tools and dies; in this respect, apart from the optimization of processing parameters, it is important to establish the most proper heat treatment conditions for the fabricated parts. In this paper, the microstructure, and some properties of H13 hot work tool steel fabricated by selective laser melting (SLM) have been evaluated after direct tempering and in quenched and tempered condition. The as-built microstructure consists of a partially tempered martensite and a much higher amount (up to 19%vol) of retained austenite (RA) compared to the quenched steel (RA<2%vol), leading to a much stronger secondary hardening during tempering. Quenching further produces a partial recovery of the solidification structure, removing the cellular/dendritic SLM structure as well as the uneven local hardness. Dilatometry highlights a much different tempering behaviour for as-built and quenched steel. Very promising fracture toughness values were measured particularly when the samples were tested with a notch plane perpendicular to the build plane (XY plane). In spite of higher hardness, the fracture toughness of tempered samples was comparable to that of quenched and tempered ones.

Keywords: tool steel; selective laser melting; quenching; tempering; dilatometry; fracture toughness

1. Introduction

AISI H13 hot work tool steel, usually used in quenched and tempered condition, shows a martensitic matrix with the dispersion of fine secondary carbides. H13 is being recognized as a good wear and erosion resistant material due to its high hardness and fracture toughness [1]. It also shows a relatively high thermal shock and thermal fatigue resistance [2–4]. These properties make H13 an excellent candidate for molds and dies [1]. H13 is usually processed by electroslag- (ESR) and vacuum arc remelting (VAR) to fulfil critical requirements such as high level of metallurgical cleanliness in terms of low vol. % of non-metallic inclusions and low segregation of alloying elements [1]. During recent years, successful trials highlighting opportunities to produce novel tool steels showing low segregation, by innovative powder metallurgical (PM) techniques such as Hot Isostatic Pressing (HIP) or Spark Plasma Sintering (SPS) have been reported [5–7]. More recently, researchers proposed Additive Manufacturing (AM), specifically Selective Laser Melting (SLM), as a cost-effective method to produce molds and dies opening opportunities for AM to involve in tooling applications [8]. According to ASTM F2792-12A, AM is defined as “the process of joining materials to make objects from 3D model data, usually layer upon layer, as opposed to subtractive manufacturing methodologies.” According to ASTM F42, for metals and alloys (AM) two process categories involving laser as the heating source, namely Powder Bed Fusion (PBF) and Direct Energy Deposition (DED). Selective Laser Melting (SLM) as a sub-category of powder bed fusion techniques (PBF) is the widely used process for the fabrication of prototype or short run dies [8]. SLM is a promising processing route to design and manufacture complex internal cavities such as conduit channels with complex geometries in one pass that cannot be achieved by traditional methods such as casting or forging. To economically balance the manufacturing process, the concept of hybrid parts for tooling is also proposed in several works [9–11]. Taking an extrusion die as an example, Hölker and Tekkaya [9] showed that channels with simple geometries may be integrated into the bridges of the die by means of conventional production techniques, whereas more complex parts (e.g., top of the mandrel) can be produced by AM. Utilizing AM, they proposed to produce small and geometrically complex parts in a hybrid die might be economically beneficial when considering the whole production cost.

Generally, the microstructure of as-built SLM processed H13 consists of a cellular/dendritic structure showing intercellular microsegregation. Results in the literature on the microstructure and mechanical properties of SLM H13 are sparse and scattered. Mertens et. al. [12] reported the SLM processed H13 consisted of martensite and large volume fractions (~15%) of retained austenite (RA). The microstructure was heterogeneous along the build height. Compressive internal stress was developed at the top surface of the part. This was explained by the martensitic transformation which causes local volume expansion in the material resulting in development of compressive stresses.

By using a preheating temperature of 400°C (i.e. higher than the martensite start temperature of H13), a fully bainitic microstructure was obtained. Moreover, the microstructure was more homogenous throughout the part. Yield strength values of the SLM H13 parts processed without powder bed preheating (i.e. 1236 ±178 MPa), as well as those processed using a preheating temperature of 400°C (i.e. 1073 ±72 MPa) were lower than that produced conventionally (i.e. 1650±10 MPa). Moreover, elongation at break for both SLM parts was almost half of that obtained for a conventionally processed H13 (i.e., ~9%). Xue [13] reported that the yield and tensile strength of SLM processed H13 was comparable to that of quenched and tempered wrought H13 (i.e., 1288±54 MPa and 1584±24 MPa respectively) while the rupture elongation of the SLM H13 was 5–6% lower than that of the wrought counterpart. Holzweissig et al. [14] reported the samples built parallel to tensile loading direction exhibited higher ultimate tensile strength (UTS) and elongation at break compared to those built perpendicular to the loading direction (i.e., 1600 MPa and 2.25% vs. 1200 MPa and 1.5% respectively). This variation was explained in view of the higher numbers of layers needed to fabricate the samples built parallel to tensile loading direction which in turn required longer processing times. Therefore, intrinsic tempering of the readily solidified material due to the repetitive heat flow to the building plate was more extensive which led to localized precipitation of secondary carbides and tempering of the highly supersaturated martensite. Other process related defects such as porosity, thermal cracking due to residual stress build up, carbon segregation to the melt pool boundaries and highly textured microstructure may become obstacles in achieving isotropy in mechanical properties of SLM processed tool steels [15]. In addition to the inherent characteristics of SLM process, the above results may also be a consequence of the complex metallurgy of tool steels, showing solid-state phase transformations during heating and cooling, which should be taken into consideration. Moreover, according to the previous experience of the authors and several other researchers [12,14,16,17], H13 produced by SLM shows substantial volume fractions of retained austenite. RA is detrimental to the tool service life because its transformation into martensite, accompanied by a volume expansion, may result in distortion or cracking of components.

Conventionally processed and PM tool steels mostly undergo austenitizing/quenching treatments before being tempered [1]. For the SLM products, heat treatment strategy may be realized without quenching because of the rapid solidification during the process [18]. However, as discussed earlier, it has to be noted that the inherent tempering due to the layer by layer deposition characteristic of SLM, might dramatically affect the microstructure of readily solidified parts thus leading to microstructural heterogeneities. Therefore, the opportunity to skip quenching should be carefully evaluated. This requires a systematic study to correlate the changes in the microstructure, phase transformations, precipitation behaviour *and mechanical properties* upon post-processing thermal treatments in SLM processed H13.

This work is an endeavour towards identifying and characterization of the microstructural features of the SLM processed H13 as well as tailoring microstructural changes and phase transformations during heat treatment (e.g. quenching and tempering or direct tempering) by the aid of dilatometry. Particular attention is devoted to the homogenization of the highly heterogeneous solidification structure of SLM processed-H13 and to obtain the best equilibrium between hardness and fracture toughness.

2. Materials and methods

AISI H13 gas-atomized (d_{10}=19µm, d_{50}=31µm, d_{90}=51µm) spherical powders (Sandvik Osprey, 0.45% C, 1.62% Mo, 5.36% Cr, 1.1% V, 0.43% Mn, 0.94% Si, Fe bal.) were used as the feedstock. Referring to a previous work of the authors [16] powders show a cellular structure featuring the microsegregation of alloying elements as a result of rapid solidification.

Standard dilatometry samples, i.e., cylinders (10mm × Ø 4mm) were processed with the SLM machine model: MCP HEK REALIZER II. The scanning was performed in an alternate-hatching pattern. Layer thickness (d) was 50µm and the hatching distance (h) was set as 120µm (Fig.1a). With each sequential scan, the scanning orientation was rotated by 90 degrees. The process was performed in a high purity argon atmosphere with 10mbar outlet pressure and an initial oxygen content less than 0.6 vol. %. Three different laser energy densities of 67J/mm^3, 100J/mm^3 and 300J/mm^3 were considered for the sample fabrication. Eq.1 defines the volumetric energy density.

$$VED = \frac{p}{v \times h \times t} \left(\frac{J}{mm^3}\right) \quad (1)$$

where *P* is the laser power (100W), *v* is the scan speed, *t* is the layer thickness and *h* is the hatch spacing in mm [19]. In the present work, the only variable to tune the energy density was the scanning speed.

Density measurements were carried out according to ASTM EB962 following the Archimedes' principle. The microstructure was characterized by optical and scanning electron microscopy. The etchant used was Nital 2% (nitric acid and ethanol). Energy dispersive X-ray spectroscopy (EDS) quantitative analysis was utilized to highlight the concentration of alloying elements in micro-segregated regions. Phase mapping on as-built samples was performed by electron backscatter diffraction (EBSD) performed using a Nordlys F detector. All Vickers micro-hardness measurements were done on the metallographic cross-sections using 100gf load (HV0.1).

The phase constitution was determined by means of X-ray diffraction (XRD) analysis using an Italstructures (IPD3000) instrument equipped with Co Kα source (λ = 0.17889 nm). Data were elaborated by the Rietveld method using MAUD (Materials Analysis Using Diffraction) software [20]. MAUD was also used to determine

mean crystallite size and the average lattice microstrain by line profile analysis using line broadening method according to the “Delft” model [20].

Dilatometric tests were carried out by a Bahr DIL 805 dilatometer. Heating was conducted under dynamic vacuum (5×10^{-4}mbar) and cooling was performed using Argon flow. The dilatometry data provide a measure of length change. In order to highlight the phase transformation temperatures or precipitation events, data were differentiated with respect to temperature [21]. Controlled and instrumented quenching and tempering experiments were also carried out using Bahr DIL 805 dilatometer.

A first batch of as built samples were austenitized at 13°C/min up to 1020°C and were held for 15min. During heating, a preheating stage at 700°C for 15min was introduced to allow a uniform temperature distribution inside the sample, just before the phase transformation of martensite into austenite. Quenching was performed at 40°C/s to room temperature. The following tempering was carried out with a heating rate of 12°C/min followed by quenching at a cooling rate of 30°C/s (see table 1 for the codes and description). A second batch of samples was only tempered. Tempering curves were determined by twice tempering (2 hours each) at different temperatures (i.e., 450°C, 500°C, 550°C, 600°C and 650°C). Vickers hardness was measured using 1Kgf (HV1) on metallographic cross-sections of the samples.

The phase transformations during tempering have been also studied by isochronal dilatometry and differential scanning calorimetry (DSC). In the first case, dilatometric samples have been heated up to 800°C at 13°C/min. DSC was carried out using Perkin Elmer DSC7 in Argon atmosphere to avoid oxidation. The mass of the specimen, cut from the cylinder, was around 50mg. Specimens were heated from room temperature to 720°C (the maximum temperature could be provided by the device) with a heating rate 10°C/min and subsequently cooled down to RT with a cooling rate of 40°C/min. The baseline was obtained by second scanning under similar experimental conditions assuming that all transformations are irreversible and completed after the 1st run. The subtracted signal evidences any phase transformation or precipitation event during the heating stage, as well as any martensitic transformation occurring on cooling.

Table 1. Samples code and description

Code	Sample description
x-AB	As-Built sample fabricated using *x* energy density (J/mm^3)
x-Q	Sample fabricated using *x* energy density (J/mm^3) and subsequently quenched
x-T-y°C	Sample fabricated using *x* energy density (J/mm^3) and subsequently tempered at temperature *y* (°C)
x-QT-y°C	Sample fabricated using x energy density (J/mm3) and subsequently quenched and tempered at temperature y (°C)

Cubic samples (7mm × 30mm × 30m*m*) were produced maintaining the same SLM parameters described earlier (Fig.1a). A part of them was subjected to quench and tempering and another batch was directly tempered using the same cycles of dilatometry tests. However, heat treatments were all carried out in a vacuum furnace (TAV Minijet). Fracture toughness samples (6mm× 3mm × 30mm) were extracted by EDM. A notch (a=3mm, $\rho = 50\mu m$) was finally wire electro-discharge machined. Regarding scan strategy (Fig.1a), one set of samples was produced in a manner that notch plane was parallel (P) to the build plane (Fig.1b), while in a second set it was normal (N) to the notch plane (Fig.1c). Plane strain fracture toughness tests for the small notched specimens were performed according to the ASTM E399. It should be noted that longitudinal stress (σ_{yy}) ahead of a notch decreases with increasing the root radii thus the stress triaxiality decreases consequently [22]. Therefore, higher stress is needed to reach the "critical stress intensity" and apparent fracture toughness (K_{app}) obtained by this method will be higher than the plane strain fracture toughness (K_{IC}) obtained with fatigue notched specimen (i.e., $\rho \rightarrow 0$).

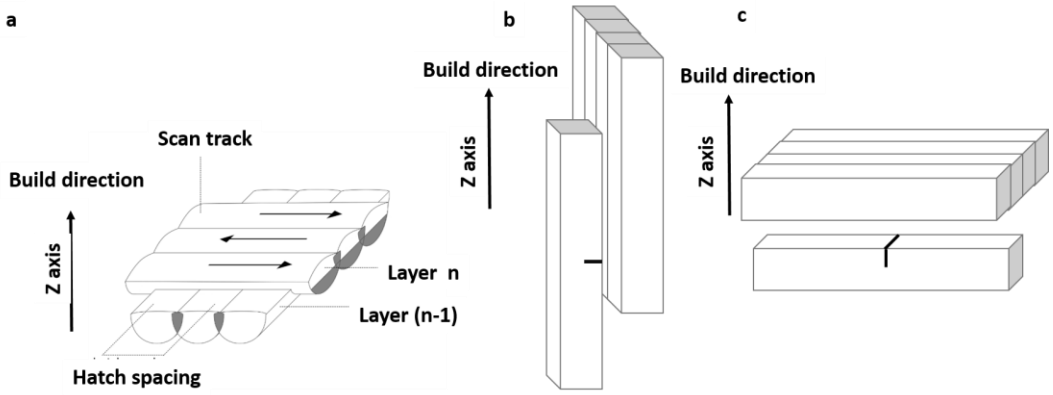

Figure 1. Schematic of a) scanning strategy, b) fracture toughness samples with the notch plane parallel to the build plane (XY plane) (P), c) fracture toughness samples with the notch plane normal to the build plane (XY plane) (N)

3. Results and Discussion

3.1 As-built Tool Steel

The microstructure of the as built samples (AB) reveals a layered structure with two distinct regions (Figs 2a-d), characterized by different etching contrast. Fairly periodic darker areas corresponding to tempered martensite alternate with brighter regions corresponding to less extensive tempering. Tempering may be revealed better by looking to the SEM micrograph (Fig. 2f) highlighting the presence of very fine secondary carbides, which are not present in the whiter areas. The microhardness measurements confirm the lower hardness of the darker regions (T, 604±12 HV0.1), compared to that of lighter martensite regions (Q, 662±14 HV0.1) which may be considered closer to an as rapidly quenched condition. As discussed by other works [23] as soon as each additional layer

is deposited, the previously deposited layers are subjected to a temperature increase due to the heat transfer from the solidifying layer towards the substrate. Therefore, up to a certain distance from the solidifying layer, the previously built layers may become tempered (i.e., inherent tempering during the SLM process). The microstructure of the SLM processed H13 consists of a cellular/dendritic structure showing intercellular micro-segregation of alloying elements a result of the rapid solidification (~10^4°C/s), characteristic of SLM process (Figs. 2e&f) [24]. The majority of pore population was found to be the interlayer porosities because of poor melting of powders specifically when a low laser energy density (Fig. 2b) was used.

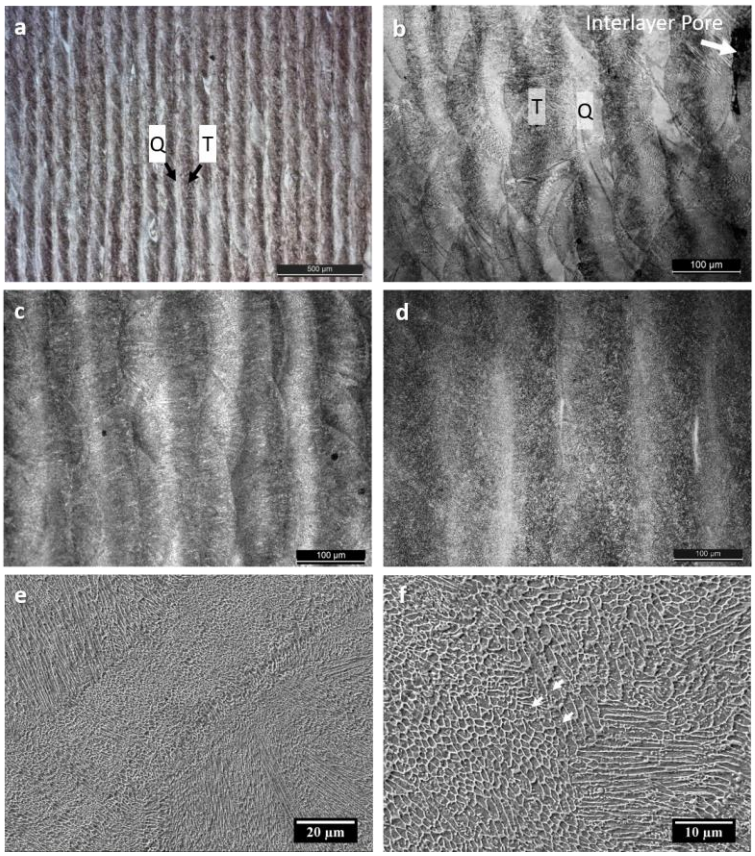

Figure 2. Side view of SLM processed samples: a) low magnification micrograph showing the SLM processed H13 structure consisted of periodic layers with different response to chemical etching namely T (tempered) and Q (quenched), b) AB sample processed with 67j/mm^3 energy density presenting interlayer pores, c) AB sample processed with 100 j/mm^3 energy density, d) AB sample processed with 300j/mm^3 energy density, e) SEM micrograph showing the cellular/dendritic structure, f) higher magnification SEM micrograph highlighting precipitations at the darker (T) zones

XRD analysis (Fig.3) on the AB specimens and the high hardness of the samples confirm the major phase constitution is martensite. A large amount of RA (i.e. a maximum of 19 vol%) was also revealed by XRD analysis. EBSD phase map (Fig.4) shows the presence of retained austenite at the cellular boundaries as a result of the chemical stabilization of austenite due to the intercellular micro-segregation of alloying elements. The origin of

such a high amount of RA and its dependence on the laser energy density is discussed in detail in the previous work of authors [16].

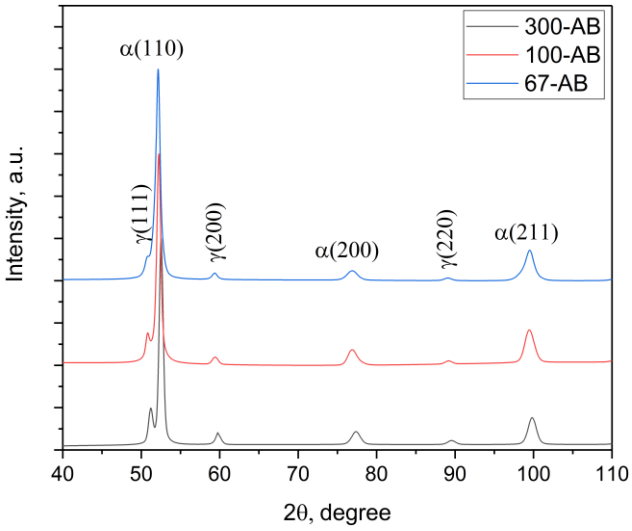

Figure 3. XRD patterns of the AB samples

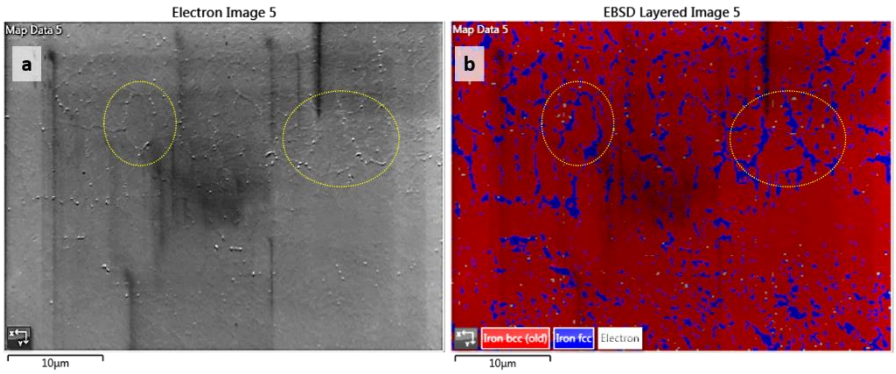

Figure 4. 300-AB sample SEM micrograph and corresponding EBSD layered image showing α (red) and γ (blue) phases, RA(γ) is found at the cellular boundaries (i.e., micro-segregated regions), hit rate: 82%

Line profile analysis results (Table 2) confirm that the crystallite size of α-Fe increases with increasing the laser energy density probably due to the lower cooling rate, while the average microstrain as a measure of the defects density (e.g. dislocations) remains nearly constant (~0.25%). The major contribution of the microstrain arises from the lattice distortion induced by the martensitic transformation [25], therefore, it is reasonable that the energy density does not affect the microstrain dramatically.

Table 2. XRD quantitative phase analysis and line profile analysis result of SLM processed sample (AB)

Laser energy density/AB sample	α-Fe mean crystallite size (d), (nm)	α-Fe mean microstrain $(\varepsilon^2)^{1/2}$	Vol% γ-Fe
67-AB	29.1±1.5	0.25	13.0±0.4
100-AB	41±1.0	0.21	17.0±0.2
300-AB	47.5±0.4	0.28	19.6±0.7

Rel. density of the specimens increases by increasing the energy density (Fig.5). Micro-hardness (HV0.1) of the samples decreases by increasing the laser energy density as a result of crystallite size coarsening (Hall-Petch relation) and increase of RA vol%. Moreover, it is expected by increasing the laser energy density the temperature rise in readily solidified layers due to the heat transfer from the solidifying layer towards the substrate becomes larger [15]. Therefore, the tempering effect becomes stronger leading to a lower microhardness. This decreasing trend is not valid when looking at the hardness values (Fig.5). The most probable reason is that the measurements could be negatively affected by the presence of an elevated level of porosity at low laser energy densities.

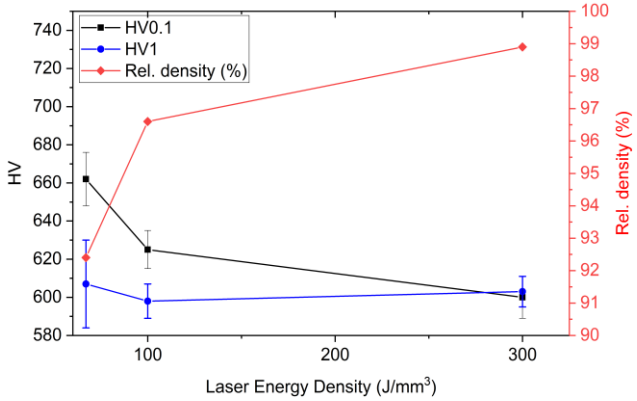

Figure 5. Rel. density, microhardness and hardness vs. laser energy density, please note that HV0.1 is an average value of those obtained from white (Q) and dark (T) areas

3.2 Heat Treatment (dilatometry analysis)

3.2.1 Quenching

Dilatometry curve of austenitization (Fig.6a) shows a linear trend during heating up to 600°C in line with the sole thermal expansion. This is further confirmed by the first derivative of length change vs. temperature (dl/dT) which is proportional to the coefficient of thermal expansion of the sample. Between 630 and 740°C, a first contraction is evident. A second contraction comprised between 845°C (Ac_1) and 887°C (Ac_3) corresponds to ferrite to austenite (α-γ) transformation. What comes before the onset of ferrite to austenite transformation is related to the tempering behavior of AB part which will be

discussed in detail later in this section. The cooling curve (Fig.6b) is characterized by the volume-expansion due to the martensitic transformation (Ms~260°C).

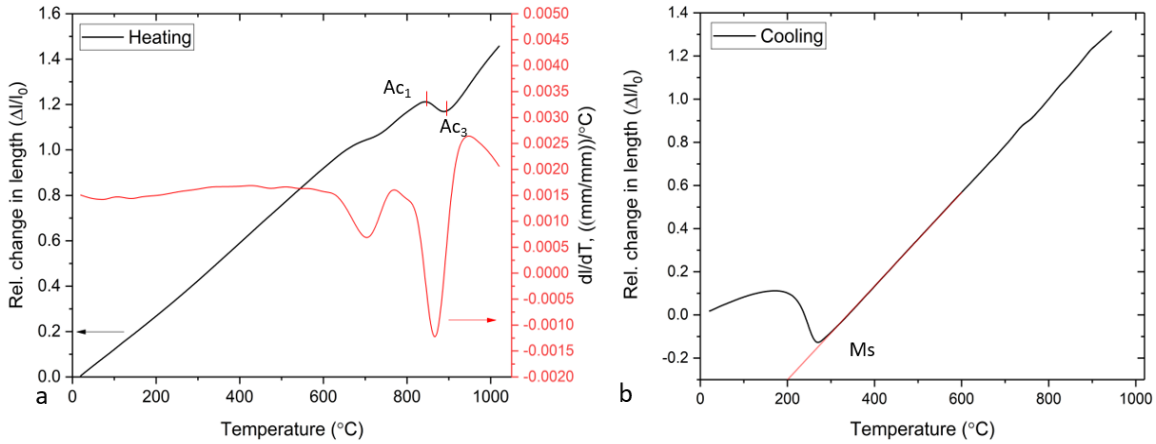

Figure 6. a) dilatometry records and length change first derivative against temperature during heating the (100-AB) and b) dilatometry records during quenching

The microstructure of the quenched sample reveals that the cellular/dendritic solidification structure is removed by diffusion, and micro-segregation is dramatically decreased (Figs.7a&b). The prior layer boundaries in the AB materials have disappeared and the newly formed prior austenite boundaries are now evident. Moreover, precipitates found in SLM structure also disappeared (Fig.7b) confirming that, as expected, also the effects of intrinsic tempering during SLM are being removed by quenching. This was also confirmed by a micro-hardness profile across the side view surface of the samples which showed relatively constant hardness values (Fig.8).

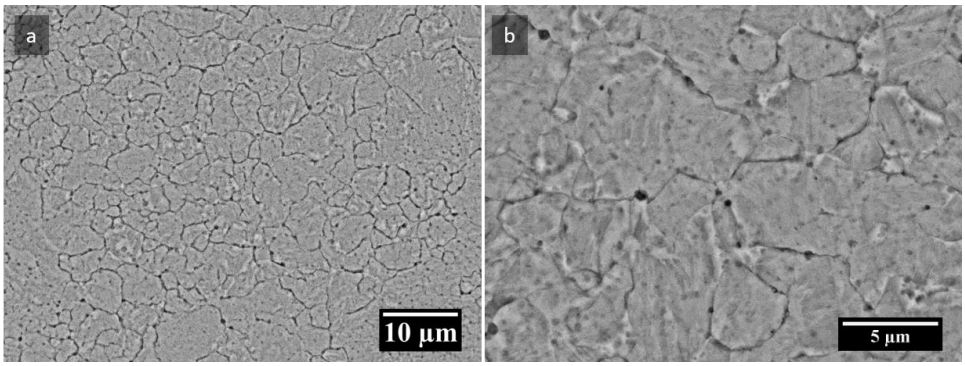

Figure 7. SEM micrographs of quenched microstructure a) removal of cellular structure and b) higher magnification micrograph showing newly formed prior austenite boundaries and absence of precipitates

The hardness after quenching is higher than previous T areas, but lower than that of previous Q zones. This last result may be explained by the lower C supersaturation of martensite assuming that, according to the equilibrium diagram, some secondary carbides will be able to precipitate during austenitizing. This would be also in agreement with the complete lack of retained austenite (less than 2%) after quenching, as revealed

by XRD analysis (Fig.9). Two further plausible reasons for the lower hardness of Q sample, seem to be the recrystallization produced by the austenitizing process and the lower dislocation density in the as quenched martensite compared to that of as-built state.

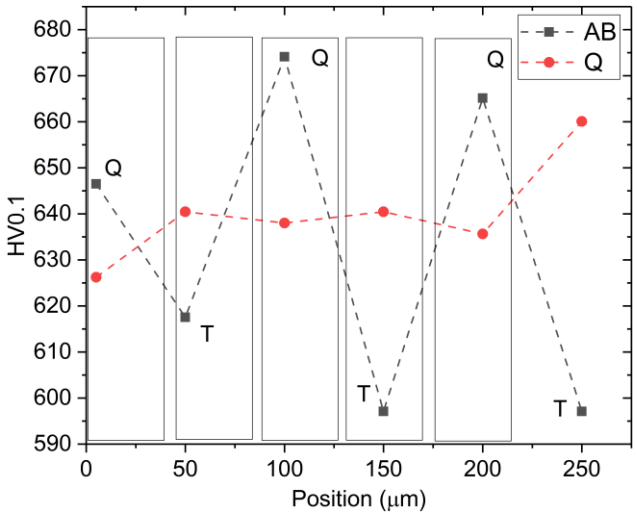

Figure 8. microhardness profiles across the metallographic cross-section of the 100-AB and 100-Q specimens

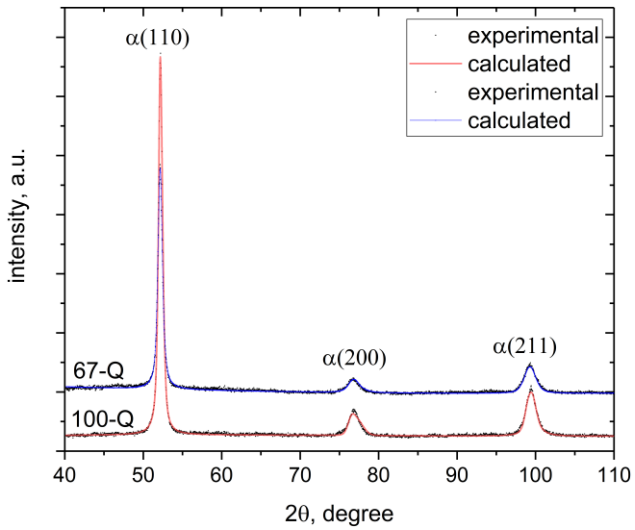

Figure 9. XRD patterns of the Q Samples, dots represent experimental data and lines represent calculated data elaborated by MAUD

It can be concluded that quenching, even if not strictly required to get a martensitic structure, leads to a beneficial recovery of the solidification structure after SLM. Moreover, it establishes the best conditions for the forthcoming tempering, i.e., homogeneous microstructure and hardness, and no retained austenite. Nevertheless, the austenitizing process does not allow a full chemical homogenizing, therefore, some related consequences can be expected in the final quenched and tempered microstructure.

3.2.2 Tempering

The AB and the Q samples were heated up to 800°C (i.e., below the onset of α-γ transformation temperature) and rapidly cooled down to room temperature. It is clearly shown that the coefficient of thermal expansion (*dl/dT*) is higher for the AB material, indicative of a higher amount of RA in this sample (Fig.10a). The dilatometry curves during heating of the Q specimen, show a very clear contraction (peak 1) between RT and 280°C corresponding to the precipitation of transition carbides (ε/η types). This is followed by another contraction (peak 2) between 450°C and 610°C which is related to the transformation/precipitation of $M_3C/M_{23}C_6$ carbides [26]. The 3rd contraction starts at 620°C showing a peak at 700°C. In Q sample the 3rd contraction can be representative of precipitation of secondary alloy carbides (i.e., MC, M_2C and M_6C) [18]. T_C (Curie temperature) is also easily detectable in dilatometry records.

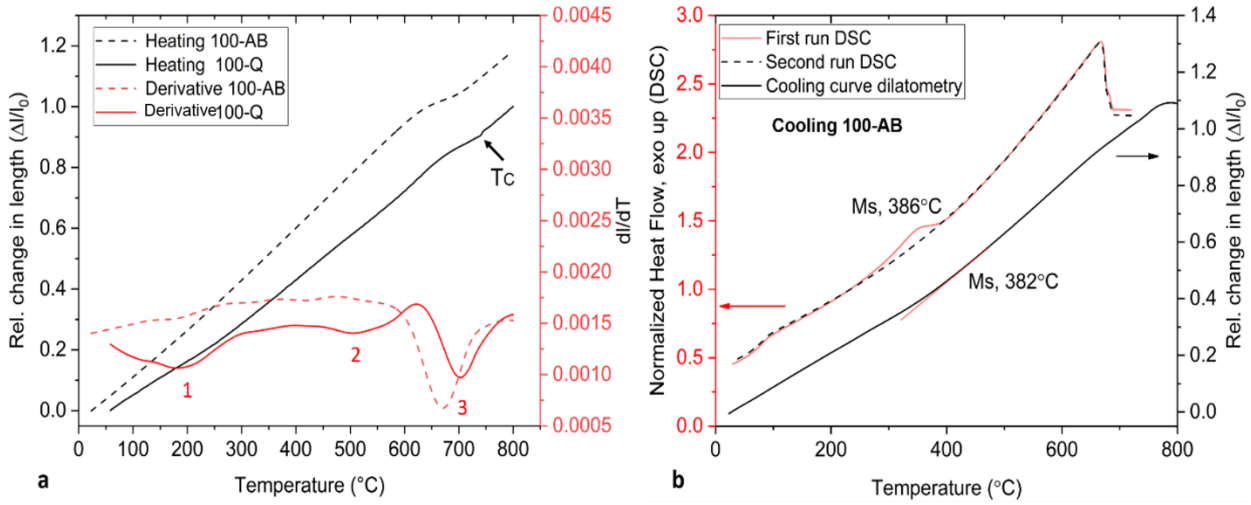

Figure 10.a) dilatometry records and the first derivative of length change against temperature during heating to 800 °C for AB and Q samples and b) dilatometric records during cooling the AB sample from 800 °C and DSC curve during cooling the AB sample after 5min holding at 720°C

A first important observation is that the 1st and 2nd peaks are not present in AB specimen. As discussed earlier, the low temperature precipitation reactions of transition carbides, have already taken place during the SLM process where the solidified layers experience significant heat transfer from the solidifying layer resulting in the tempering of the martensite (see Fig.2). Therefore, these reactions (if any) could not contribute to a pronounced contraction during tempering. On the other hand, the 3rd contraction peak is evident for the AB sample and its intensity is almost twice that observed in the Q sample. Tc cannot be detected in AB sample which can be a result of interference with the large contraction peak due to carbides precipitation. Looking to the peak intensity and considering that the current AB samples show a large amount of RA, contraction might represent the simultaneous effect of the *i)* decomposition of highly alloyed retained austenite, resulting from a strong micro-segregation in SLM processed H13, into low

alloyed austenite and carbides, and *ii)* precipitation/transformation of secondary carbides directly from the martensite. During isochronal tempering of martensitic steels with increased carbon contents, retained austenite decomposition and carbide precipitation (i.e. tempering reactions) usually overlap [27]. Further, in contrast to retained austenite decomposition in low carbon steel which causes a volume increase, Caballero et al.[28] showed that the decomposition of highly alloyed retained austenite may cause a volume decrease, which is in agreement with the present results and that of Lerchbacher et al. [29]. This evidence can be further justified by looking to the onset temperature of 3rd contraction peak in AB sample that is shifted to a lower temperature compared to the Q specimen. According to present data, precipitation of secondary carbides from austenite seems to have a faster kinetics than that form martensite, in agreement with the higher driving force related to strongly microsegregated intercellular austentite.

It is possible to postulate that for the AB sample the peak 3 contraction is the cumulative effect of two reactions, namely decomposition of retained austenite into an austenite less rich in microsegregated alloying elements (e.g. Mn, Mo, V and C) and the precipitation of carbides ($\gamma \rightarrow \gamma_{\downarrow al.el.}^{\downarrow \%c} + K$), and the precipitation of secondary carbides from the martensite. Upon cooling down the AB sample, the newly formed decomposed austenite transforms into martensite ($\gamma_{\downarrow al.el.}^{\downarrow \%c} \rightarrow \alpha'$) as displayed by DSC and dilatometric curves (Fig 10b). Further, Ms Temperature is increased to a higher temperature compared to that of Q sample suggesting that the RA is changed to a less stable condition (i.e., low alloyed RA). The martensitic transformation was better highlighted by the aid of DSC analysis, where a clear exothermic peak is evident upon cooling down the AB sample from 720° C (5min holding) to room temperature (Fig.10b). The difference in M_S temperature can be related to the different final temperatures reached in DSC and Dilatometry tests. Microstructures after this treatment differ significantly for the AB and Q material. The quenched specimen shows a massive precipitation of carbides distributed rather homogenously within the grains, some preferential precipitation on grain boundaries can be easily seen (Figs.11a&b). On the other hand, in the AB material, the microstructure after SLM is still preserved. Carbides preferentially precipitated on the cellular boundaries, in some regions the carbides are in the form of clusters resembling the prior melt pool/layer boundaries in AB sample where the maximal segregation of alloying elements occurs (Fig.11c) [30]. These areas (arrow in Fig.11d) are Mo and Mn-rich (table 3) which are the heavier alloying elements. Therefore, the thermal stability of the cellular structure can be described in the light of low mobility and micro-segregation of these substitutional alloying elements during the solidification [18]. The thermal stability of the cellular structure and retained austenite may significantly influence the tempering behaviour of the AB parts which is discussed later in this work.

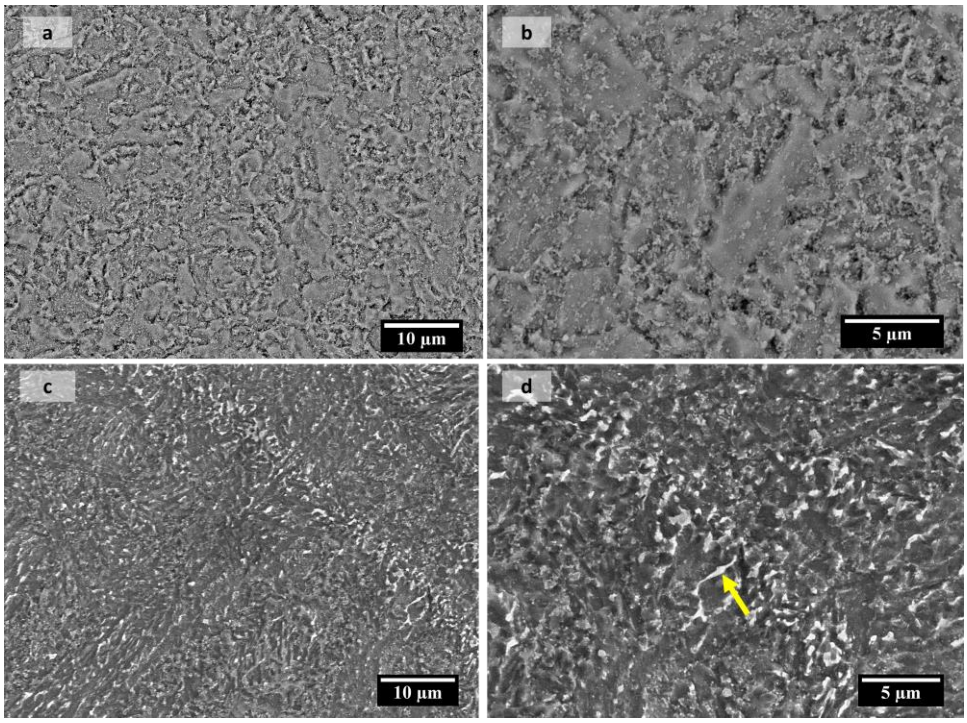

Figure 11. SEM micrographs a) showing uniform dispersion of precipitates in quenched sample subjected to heating up to 800°C, b) higher magnification micrograph, c) preferential precipitation and stability of cellular structure in the AB sample subjected to heating up to 800°C and d) higher magnification micrograph used for the EDS spot analysis (results reported in table 3)

Table 3. EDS spot analysis results on macroaggregated area addressed by the arrow in Fig.11d

Element	Si	V	Cr	Mo	Mn	Fe
wt.%	0.8 ±0.1	1.1 ±0.1	6.1±0.2	2.3±0.1	0.9±0.1	86.1±0.2

3.2.3 Quenching and Tempering vs. Tempering

The dilatometry curves recorded during the conventional heat treatment of Q and AB samples, double isothermally tempered at 600°C, are shown in Fig.12. The curves related to QT samples (Fig.12a) show a net contraction at the austenitization temperature as a result of diffusion-controlled replacement of the cellular/dendritic structure with equiaxed grains of newly formed austenite (as seen in Fig.7a) and dissolution of alloying elements in austenite. There is a slight contraction at the first of tempering (1st holding stage) representative of transformation/precipitation of secondary carbides. The cooling curve does not show any clear martensitic transformation confirming the absence of RA after quenching (Fig.12b). In the second stage of tempering (2nd holding stage), contraction is less evident compared to the 1st one, confirming that no significant precipitation occurs. On the contrary, the 1st holding stage for the ABT accompanies by a large contraction (Fig.12c), in agreement with higher intensity of peak 3 recorded during isochronal tempering (Fig.10a). Referring to previously presented results, this contraction is due to

the combined effect of decomposition of retained austenite and precipitation of secondary carbides from the martensite which is confirmed by a clear martensitic transformation during cooling (Fig.12d).

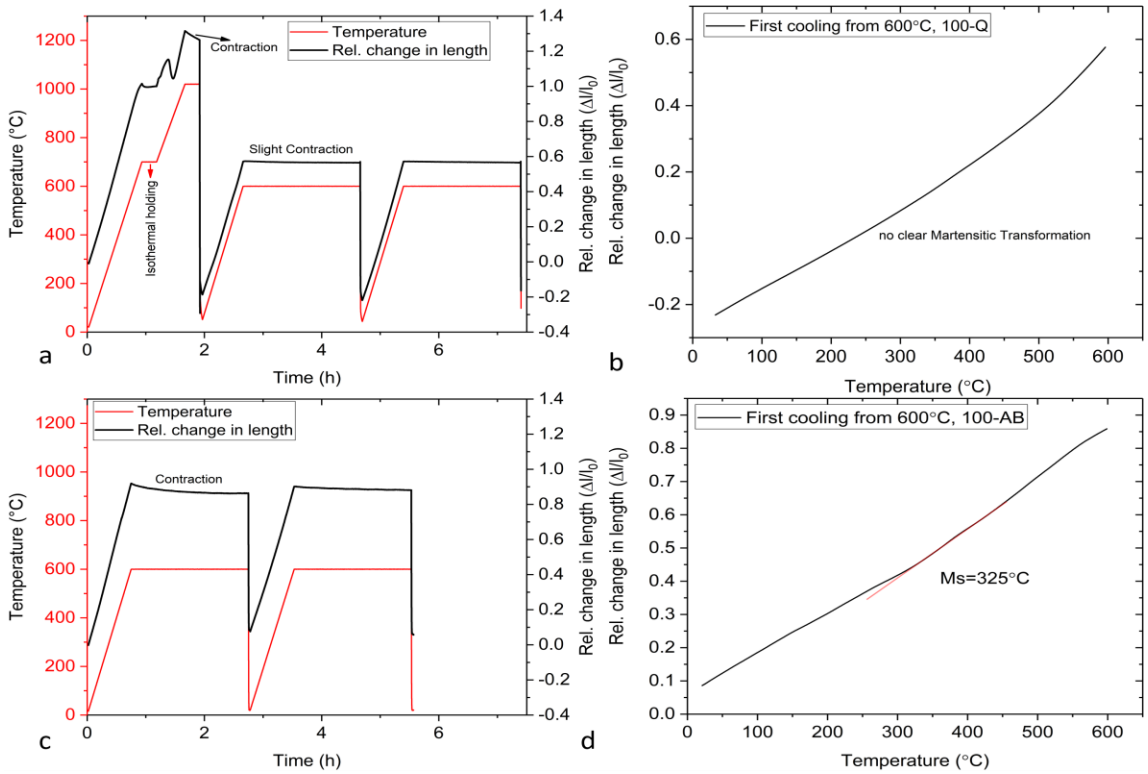

Figure 12. dilatometry curves of a) austenitizing quenching followed by double tempering at 600°C, b) first cooling from 600°C for Q sample, c) direct double tempering of the AB sample and d) first cooling from 600°C for the AB sample

XRD patterns of ABT and QT specimens after tempering at 500 and 600°C are shown in Fig.13. As expected, QT does not contain retained austenite at both 500°C and 600°C tempering temperatures. On the other hand, no RA was found in the ABT tempered at 600°C, whilst around 8 vol% RA is evident in the ABT tempered at 500°C.

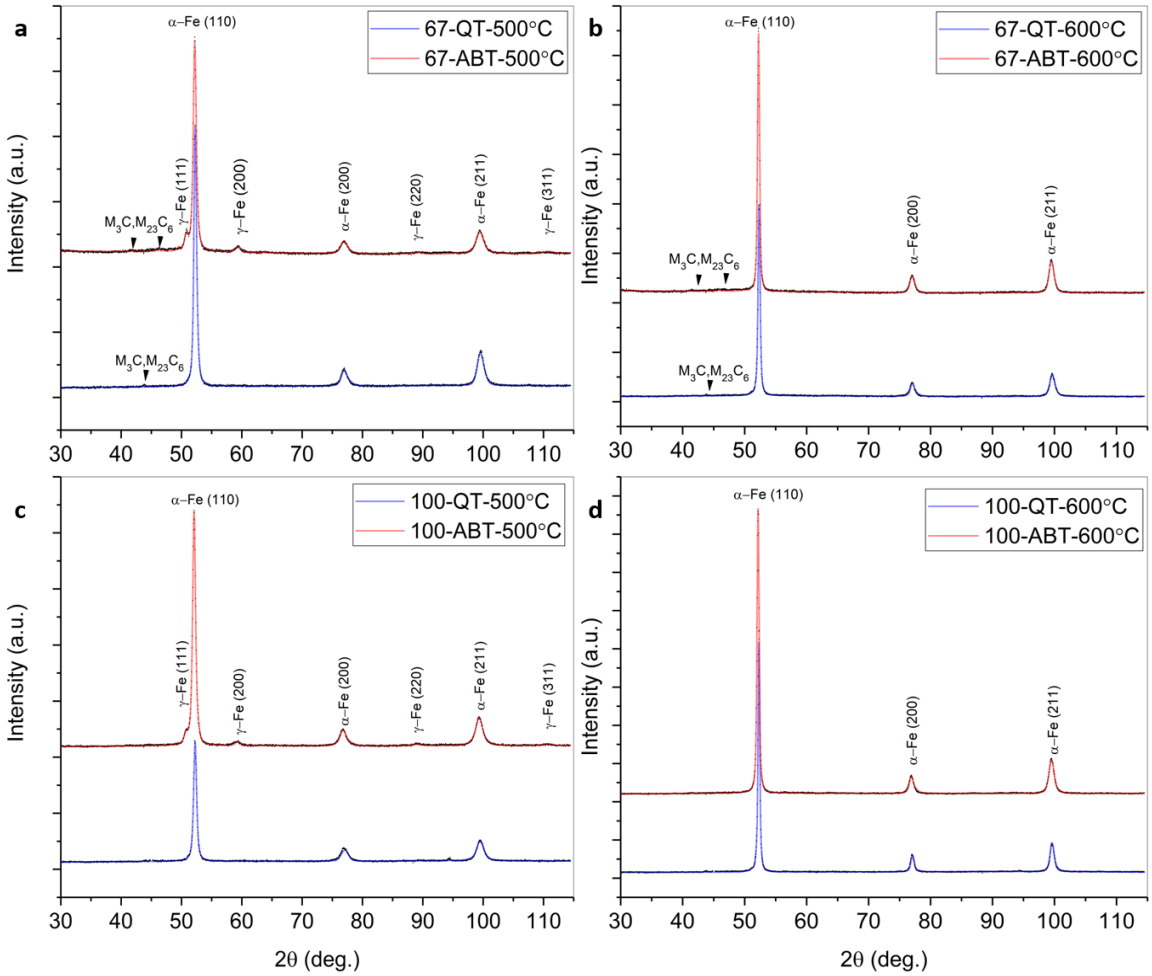

Figure 13. XRD patterns of directly tempered (ABT) and quenched tempered (QT) samples produced with different laser energy densities a) 67 J/mm^3 double tempered at 500°C, b) 67 J/mm^3 double tempered at 600°C, c) 100J/mm^3 double tempered at 500°C and d) 100 J/mm^3 double tempered at 600°C, dots represent experimental data and lines represent calculated data elaborated by MAUD

In ABT, the cellular/dendritic arrangement can still be observed even after tempering at 600 °C (Fig.14a), where a continuous network of carbides in the microstructure is observed. The continuous network resembles prior melt pool boundaries where segregation of alloying elements occurs during rapid solidification. Indeed, after double tempering at 650°C, the cellular structure seems to be largely recovered (Fig. 14b) but there are still plenty of regions characterized by a continuous network of carbides. Apart from preferential precipitations on the melt pool boundaries, secondary carbides distribution within the martensite seems to be fine and homogenous (Fig14c). In QT samples, at any tempering temperature, the microstructure is homogeneous consisting of tempered martensite with the dispersion of very fine secondary carbides. Some interconnected network of carbides is also found on the prior austenite boundaries (Figs14d-f) confirming that Q does not completely delete the solidification structure in

particular, microsegregations that would need an homogenization annealing at a higher temperature, for a longer time.

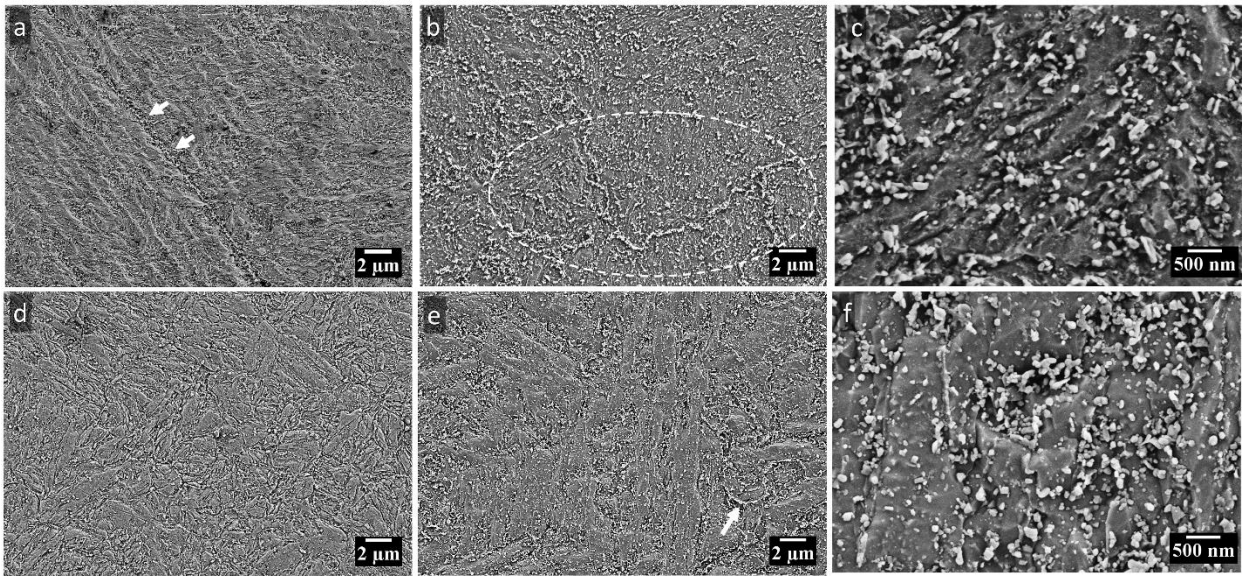

Figure 14. microstructure of a) ABT-600°C, b) ABT-650°C, c)higher magnification micrograph showing the dispersion of fine secondary carbides in ABT tempered at 650°C, d) QT-600°C, e) QT-650°C, arrow points to an interconnected carbide network, f) higher magnification micrograph showing the dispersion of fine secondary carbides in QT tempered at 650°C

The initial structure of the AB samples comprising periodically tempered (T) and quenched (Q) regions (See Fig.2) is largely homogenized upon tempering at 600°C and above. This was also confirmed by the micro-hardness profiles on the surface showing a relatively linear trend (Fig. 15).

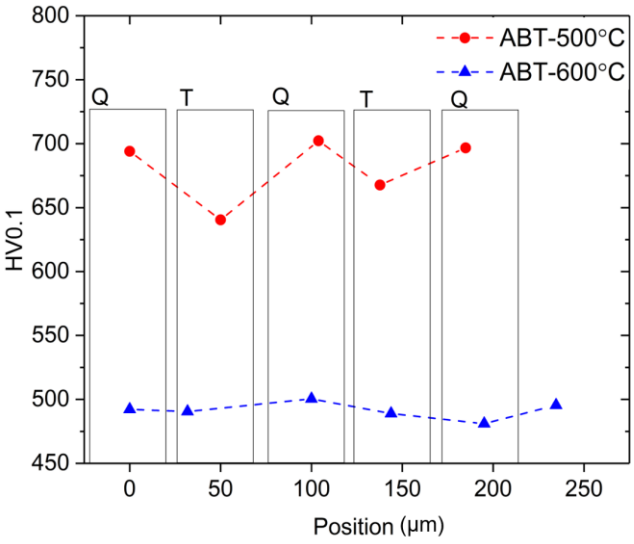

Figure 15. microhardness profiles across the metallographic cross-section of the ABT samples tempered at 500°C and 600°C

3.3 Tempering curves

Tempering curves of AB and Q samples are depicted in Fig.16, together with that of a spark plasma sintered (SPS) PM H13 [31] produced with the same powders. PM tool steel was subjected to austenitization and quenching, identical to that reported in this work, before tempering.

Two distinct differences can be noticed in the tempering curves between ABT and both SPS (QT) and QT. *i)* AB samples show a significantly lower starting hardness compared to the Q specimen, *ii)* AB shows a pronounced secondary hardening peak shifted to higher temperatures (i.e. 500-550°C) compared to those quenched and tempered (i.e. 450-500°C). In spite of the very fine microstructure (Table 2), lower starting hardness of AB is a consequence of the high amount of RA and the presence of partially tempered martensite (Fig.2). In a conventionally produced tool steel as well as the quenched PM tool steel reported here, the hardness declines by tempering at low tempering temperatures is mainly due to the recovery of dislocations, relaxation of highly distorted supersaturated martensite and precipitation of transition carbides from the martensite (peaks 1 and 2 in Fig. 10a). The SLM samples have already undergone localized and repetitive tempering during the SLM process. According to the micro-hardness profile results (Fig. 15), the average temperature rise in the readily solidified layers should have been more than 500°C, since at this tempering temperature the periodic hardness variations still exist, meaning that the tempered regions have been exposed to a higher tempering temperature (>500°C) during the SLM process [32]. This can be also confirmed by looking to the dilatometry curves in Fig.10a where the first contraction peak for the AB occurs near 630°C during isochronal heating. The decomposition of RA causes a marked hardness increase above 550°C, giving rise to a well pronounced secondary hardening. For the two other samples, austenitizing at 1020 °C followed by quenching results in a rather homogenous microstructure comprising supersaturated primary martensite. Therefore, they show similar tempering behaviour seen in conventionally produced H13 tool steels [23]. The higher starting hardness of SLM (Q) with a prior austenite grain size (d_{PAG}) of less than 4 µm (Fig.7b) compared to that of SPS processed quenched sample (d_{PAG}=4.1 ±0.5[33,34]) can be described by the finer microstructure of the former (i.e., Hall-Petch strengthening).

According to the obtained data in Fig.16, tempering of SLM components in the AB state will require different temperature compared to the same component after Q, if the same hardness must be obtained. Since the main reason is the high amount of RA, a possible solution to avoid higher tempering temperature is to (partially) transform RA before tempering by means of a cryogenic treatment.

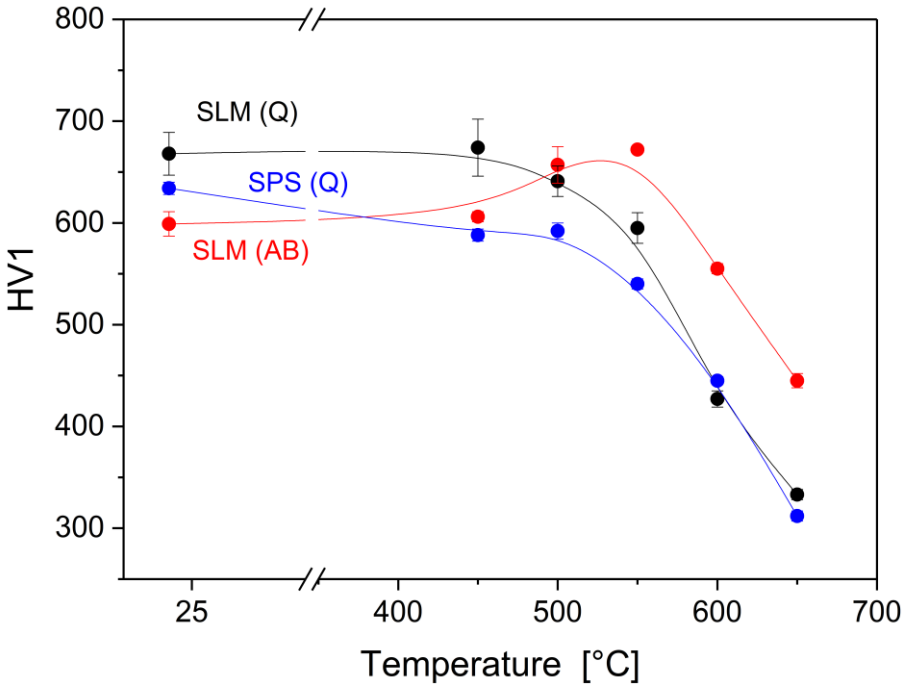

Figure 16. Tempering curves of the SLM processed (QT and ABT) and SPS (QT) samples

3.4 Fracture Toughness

Fracture toughness tests have been carried out on samples processed with 300J/mm^3 (Fig.17) showing the highest rel. densities (i.e. 98.9%). The hardness of QT samples was lower than that of ABT ones (~390 HV1 vs. ~460 HV1). Fig.17 shows the apparent fracture toughness (K_{app}) vs. hardness for the specimens. The K_{app} values for both samples is higher when the build plane is normal to the notch plane. K_{app} of the QT samples (71.3±3.2 MPam$^{1/2}$) is higher than the ABT (67.5±2.8 MPam$^{1/2}$) when the build plane is parallel (P) to the notch plane. Surprisingly, in spite of its higher hardness, K_{app} of the ABT sample (85.3±2.1 MPam$^{1/2}$) is higher than its QT counterpart (80.3±1.3 MPam$^{1/2}$) when the crack plane is normal to the building plane (N). The situation is inverted considering the P samples. It can be observed that the lower K_{app} values of SLM samples can be compared to the SPS H13 (Rel. density 99.4%) with a hardness of 425 HV1 and a K_{app} equal to 75.0±3.0 MPa×m$^{-1/2}$)[35]

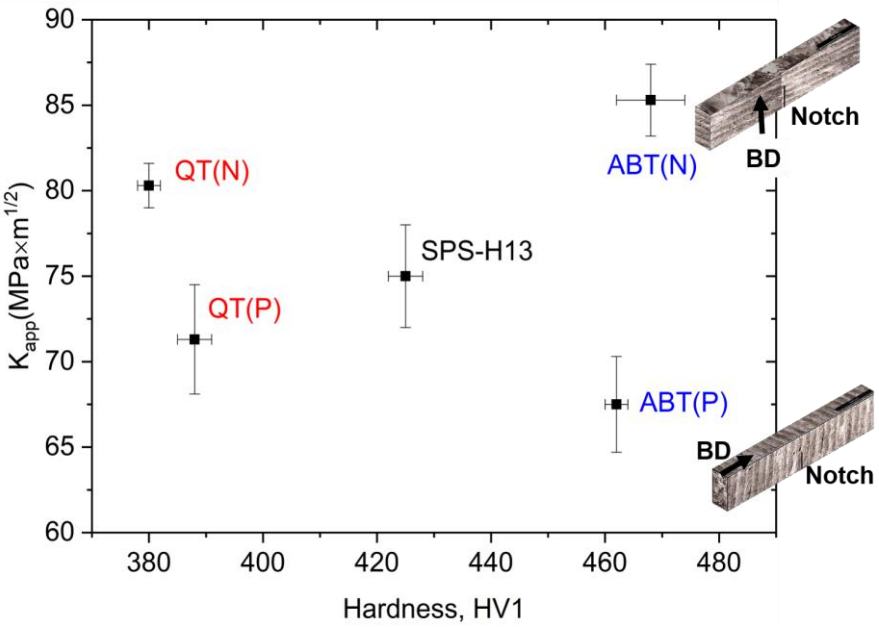

Figure 17. Hardness vs. fracture toughness of SLM processed (laser energy density: 300J/mm^3) samples: (QT) and (ABT), results obtained from the SPS produced sample is presented for comparison

Looking to the crack propagation paths, in addition to the process related defects such as pores and inclusions, it can be postulated that the prior melt pool and/or layer boundaries play a role on the crack propagation in directly tempered samples. Layer boundaries with continuous carbide networks resultant of strong segregation of alloying elements (see Figs. 14a&b) act as preferential crack propagation paths (Fig 18a, crack path in dashed square and Fig.18b) when the notch plane is parallel to the build plane (P). Therefore, in this case, a lower fracture toughness is expected. This phenomenon was also observed in a number of tested QT specimens, even if in a less evident way. When the notch surface is normal to the build plane (N), the prior melt pool and/or layer boundaries tend to arrest the propagating crack and deviate the crack path. This behavior was seen in both heat treatment conditions (Fig. 18c, black arrow). Moreover, the formation of secondary cracks with a plane normal to the notch plane at the melt pool boundaries is evident (Fig.18c, white arrow). These cracks may form during loading due to the lower fracture toughness of the part in the weaker (P) configuration (i.e., when the notch plane is parallel to the building plane). Secondary cracks may reduce the through-thickness constraint and decrease the “main crack” driving force leading to an increase in the fracture toughness by extrinsic toughening mechanisms [36]. The positive effect of the layer and/or melt pool boundaries in (N) configuration should be more pronounced in the ABT samples because austenitizing was skipped for these samples and the structure of the layer and/or melt pool boundaries is more similar to the AB state. This can explain the higher fracture toughness of the ABT compared to the QT one. From the micromechanics viewpoint, the formation of secondary cracks leads to a stress relaxation which should cause a sudden load drop in displacement-controlled loading. Load drops

(1 & 2) in load-displacement records (Fig.19) are evident and confirm the formation of secondary cracks in the specimen in line with the metallographic observations.

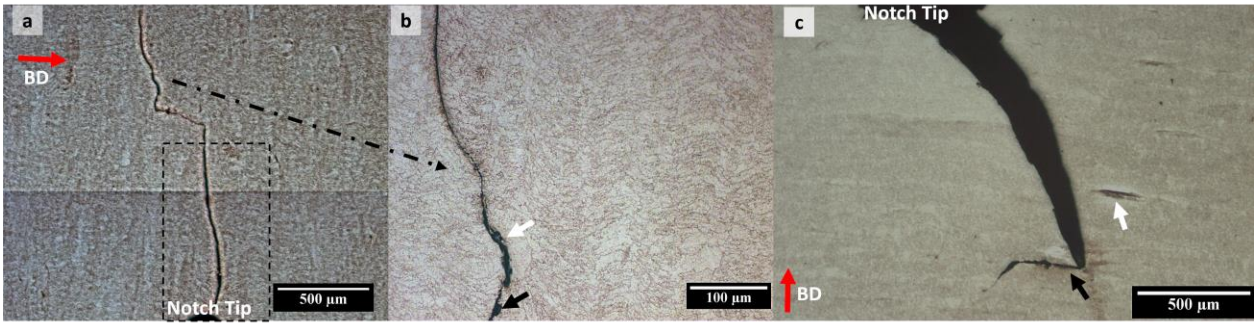

Figure 18. Crack propagation paths, a) ABT with notch plane parallel to the building plane (ABT(P)), b) higher magnification micrograph showing crack propagation through a melt pool boundary, white arrow indicates an inclusion and solid black arrow is pointing at a pore, and c) QT with notch plane normal to the building plane (QT(P)) showing crack arrest (black arrow), deviation and the formation of secondary cracks (white arrow)

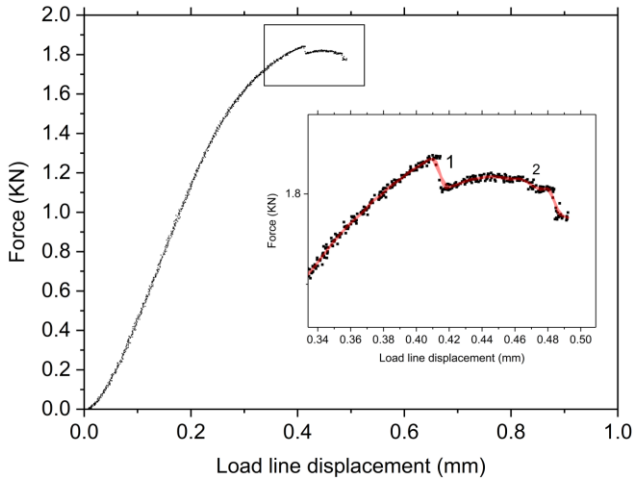

Figure 19. A test record for QT (N) sample showing sudden load drops (1 and 2) in the final stages of loading

The fracture surface of QT (P) is very rough (Fig. 20a). At the “near notch” area, the fracture surface is characterized by quasi-cleavage fracture showing the presence of dimples (Fig.20b). QT(N) sample shows a relatively flat fracture surface, the fracture surface highlights the formation of secondary cracks (marked by SC in Fig.20c) with planes perpendicular to the notch plane. “Near notch” fracture surface shows plenty of dimples indicating a micro ductile fracture, while some isolated cleavage facets are also present on the fracture surface (Fig.20d). ABT(P) shows a flat fracture surface while large delaminations, probably representing preferential crack growth at the prior melt boundaries, are evident on the fracture surface (Fig.19e). The occurrence of delamination is also seen in ABT(N). However, the size of the delamination is much finer in ABT(N)

(Fig.20g). Moreover, the presence of secondary cracks on the fracture surface is evident. The near notch surface in both ABT samples is characterized by cleavage facets together with a very small fraction of fine dimples (Figs. 20f&h).

The lower yield strength of the QT sample allows larger plastic deformation at the notch tip sufficient for dimple formation, by decohesion along matrix and evenly dispersed carbides or some larger inclusions (insert in Fig. 20b) interface, before fracture completes by cleavage [37]. The cleavage fracture can be attributed to the higher hardness (higher yield strength) of the ABT samples which results in a small difference between the cleavage stress and yield stress [37]. Therefore, negligible plastic deformation is needed to increase the local stress at the tip of the notch from the level of the yield stress to the cleavage fracture stress level. Moreover, closely spaced and/or interconnected network of fine carbide particles serve as preferential sites for the microvoid nucleation (marked by an arrow in Fig.20h) immediately followed by the transgranular fracture [38].

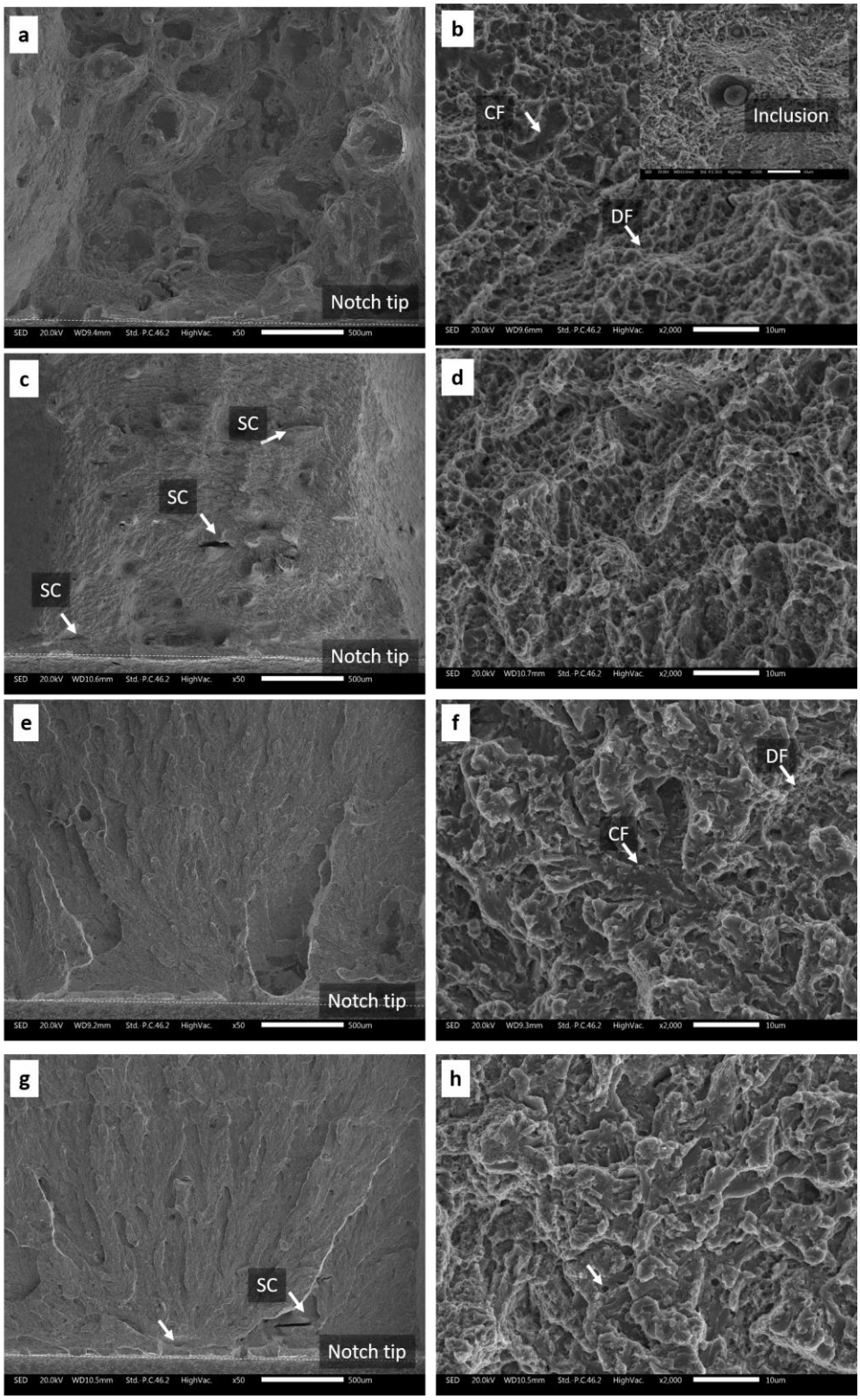

Figure 20. SEM micrographs of Fracture surfaces, a) QT(P), b) “near notch surface “ higher magnification micrograph (insert showing inclusions), c) QT(N), d) “near notch surface “ higher magnification micrograph, e) ABT(P), f) “near notch surface “ higher magnification micrograph, g) ABT(N) and h) “near notch surface “ higher magnification micrograph, arrow pointing to a micro-void

4. Conclusions

- The SLM process of H13 tool steel produces a heterogeneous cellular/dendritic microstructure showing segregation of the heavy alloying elements at the melt pool boundaries and micro-segregation at the cellular boundaries as a result of rapid solidification.
- Heat transfer from the solidifying layers to the readily solidified ones causes partial un-controlled tempering of those layers. This is highlighted by a non uniform local microhardness.
- Higher laser energy density leads to lower porosity and a higher amount of retained austenite.
- Austenitizing for 15min at 1020°C causes a partial recovery of the solidification microstructure. This is confirmed by the presence of an equiaxed martensitic microstructure after quenching. Quenching leads to a martensitic microstructure with less than 2% RA.
- QT samples showed similar behaviour compared to the PM tool steels as well as conventionally produced ones. Hardness decreased as the tempering temperature increased; secondary hardening occurred nearly at 500°C.
- Direct tempering of AB samples leads to the decomposition of retained austenite and secondary carbides precipitation above 550°C, while lower temperature transformations already occur during SLM.
- The secondary hardness peak in ABT is more pronounced and shifted to higher temperature with respect to the QT samples mainly due to the decomposition of the large volume of retained austenite. This feature might open the way to exploit the direct tempering of the SLM processed H13 in high-temperature applications which require high hardness and hot hardness.
- The measured fracture toughness values are acceptable. Fracture toughness is lower when the sample tested with a notch plane parallel to the building plane because of the preferential crack propagation through the prior melt pool boundaries, i.e., preferred carbide precipitation sites. On the other hand, the enhanced fracture toughness for samples with the notch plane normal to the build plane is explained by the formation of secondary cracks perpendicular to the original crack plane.
- Despite their higher hardness, the fracture toughness of ABT sample was comparable to the QT. Fracture toughness of the ABT samples was even higher than QT one when the pre-crack plane was normal to the building plane.

Acknowledgement

Authors are thankful to Dr. Raveendra Siriki for the EBSD analysis.

The raw/processed data required to reproduce these findings cannot be shared at this time as the data also forms part of an ongoing study.

References

[1] G.A. Roberts, R. Kennedy, G. Krauss, Tool steels, ASM international, 1998.
[2] L.-Å. Norström, M. Svensson, N. Öhrberg, Thermal-fatigue behaviour of hot-work tool steels, Met. Technol. 8 (1981) 376–381. doi:10.1179/030716981803275947.
[3] H. Andersson, Thermal fatigue and soldering experiments of additively manufactured hot work tool steels, Karlstad University, 2018. http://kau.diva-portal.org/smash/get/diva2:1237223/FULLTEXT01.pdf.
[4] M. Salem, Effect of aluminizing and oxidation on the thermal fatigue damage of hot work tool steels for high pressure die casting applications, Int. J. Fatigue. 119 (2019) 126–138. doi:https://doi.org/10.1016/j.ijfatigue.2018.09.018.
[5] O. Grinder, The HIP way to make cleaner, better steels, Met. Powder Rep. 62 (2007) 16–22. doi:10.1016/S0026-0657(07)70190-X.
[6] A. Kasak, E.J. Dulis, Powder-Metallurgy Tool Steels, Powder Metall. 21 (1978) 114–123. doi:10.1179/pom.1978.21.2.114.
[7] M. Pellizzari, A. Fedrizzi, M. Zadra, Influence of processing parameters and particle size on the properties of hot work and high speed tool steels by Spark Plasma Sintering, Mater. Des. 32 (2011) 1796–1805. doi:10.1016/j.matdes.2010.12.033.
[8] D.D. Gu, W. Meiners, K. Wissenbach, R. Poprawe, Laser additive manufacturing of metallic components: materials, processes and mechanisms, Int. Mater. Rev. 57 (2012) 133–164. doi:10.1179/1743280411Y.0000000014.
[9] R. Hölker, A.E. Tekkaya, Advancements in the manufacturing of dies for hot aluminum extrusion with conformal cooling channels, Int. J. Adv. Manuf. Technol. 83 (2016) 1209–1220. doi:10.1007/s00170-015-7647-4.
[10] R. Hölker, A. Jäger, N. Ben Khalifa, A.E. Tekkaya, Controlling heat balance in hot aluminum extrusion by additive manufactured extrusion dies with conformal cooling channels, Int. J. Precis. Eng. Manuf. 14 (2013) 1487–1493. doi:10.1007/s12541-013-0200-1.
[11] M. Merklein, D. Junker, A. Schaub, F. Neubauer, Hybrid Additive Manufacturing Technologies – An Analysis Regarding Potentials and Applications, Phys. Procedia. 83 (2016) 549–559. doi:10.1016/j.phpro.2016.08.057.
[12] R. Mertens, B. Vrancken, N. Holmstock, Y. Kinds, J.-P. Kruth, J. Van Humbeeck, Influence of Powder Bed Preheating on Microstructure and Mechanical Properties of H13 Tool Steel SLM Parts, Phys. Procedia. 83 (2016) 882–890. doi:10.1016/j.phpro.2016.08.092.
[13] L. Xue, 17 - Laser consolidation: a rapid manufacturing process for making net-shape functional components, in: J. Lawrence, J. Pou, D.K.Y. Low, E. Toyserkani (Eds.), Adv. Laser Mater. Process., Woodhead Publishing, 2010: pp. 492–534. doi:10.1533/9781845699819.6.492.

[14] M.J. Holzweissig, A. Taube, F. Brenne, M. Schaper, T. Niendorf, Microstructural Characterization and Mechanical Performance of Hot Work Tool Steel Processed by Selective Laser Melting, Metall. Mater. Trans. B. 46 (2015) 545–549. doi:10.1007/s11663-014-0267-9.
[15] H. Chen, D. Gu, D. Dai, C. Ma, M. Xia, Microstructure and composition homogeneity, tensile property, and underlying thermal physical mechanism of selective laser melting tool steel parts, Mater. Sci. Eng. A. 682 (2017) 279–289. doi:10.1016/j.msea.2016.11.047.
[16] F. Deirmina, B. AlMangour, D. Grzesiak, M. Pellizzari, H13–partially stabilized zirconia nanocomposites fabricated by high-energy mechanical milling and selective laser melting, Mater. Des. 146 (2018) 286–297. doi:10.1016/j.matdes.2018.03.017.
[17] R. Colaço, R. Vilar, Stabilisation of retained austenite in laser surface melted tool steels, Mater. Sci. Eng. A. 385 (2004) 123–127. doi:10.1016/j.msea.2004.06.069.
[18] J. Krell, A. Röttger, K. Geenen, W. Theisen, General investigations on processing tool steel X40CrMoV5-1 with selective laser melting, J. Mater. Process. Technol. 255 (2018) 679–688. doi:10.1016/j.jmatprotec.2018.01.012.
[19] B. AlMangour, D. Grzesiak, J.-M. Yang, Nanocrystalline TiC-reinforced H13 steel matrix nanocomposites fabricated by selective laser melting, Mater. Des. 96 (2016) 150–161. doi:10.1016/j.matdes.2016.02.022.
[20] L. Lutterotti, S. Matthies, H.-R. Wenk, A.S. Schultz, J.W.R. Jr, Combined texture and structure analysis of deformed limestone from time-of-flight neutron diffraction spectra, J. Appl. Phys. 81 (1997) 594–600. doi:10.1063/1.364220.
[21] C. García de Andrés, F.G. Caballero, C. Capdevila, L.F. Álvarez, Application of dilatometric analysis to the study of solid–solid phase transformations in steels, Mater. Charact. 48 (2002) 101–111. doi:10.1016/S1044-5803(02)00259-0.
[22] B.-W. Lee, J. Jang, D. Kwon, Evaluation of fracture toughness using small notched specimens, Mater. Sci. Eng. A. 334 (2002) 207–214. doi:10.1016/S0921-5093(01)01804-4.
[23] J. Mazumder, J. Choi, K. Nagarathnam, J. Koch, D. Hetzner, The direct metal deposition of H13 tool steel for 3-D components, JOM. 49 (1997) 55–60. doi:10.1007/BF02914687.
[24] B. Zheng, Y. Zhou, J.E. Smugeresky, J.M. Schoenung, E.J. Lavernia, Thermal Behavior and Microstructural Evolution during Laser Deposition with Laser-Engineered Net Shaping: Part I. Numerical Calculations, Metall. Mater. Trans. A. 39 (2008) 2228–2236. doi:10.1007/s11661-008-9557-7.
[25] F. Christien, M.T.F. Telling, K.S. Knight, Neutron diffraction in situ monitoring of the dislocation density during martensitic transformation in a stainless steel, Scr. Mater. 68 (2013) 506–509. doi:10.1016/j.scriptamat.2012.11.031.
[26] M. Pellizzari, A. Molinari, Deep cryogenic treatment of cold work tool steel, in: Proc. 6th Int. Tool. Conf., 2002: pp. 657–669.
[27] S. Primig, H. Leitner, Separation of overlapping retained austenite decomposition and cementite precipitation reactions during tempering of martensitic steel by means of thermal analysis, Thermochim. Acta. 526 (2011) 111–117. doi:10.1016/j.tca.2011.09.001.

[28] F.G. Caballero, C. García-Mateo, C.G. de Andrés, Dilatometric Study of Reaustenitisation of High Silicon Bainitic Steels: Decomposition of Retained Austenite, Mater. Trans. 46 (2005) 581–586. doi:10.2320/matertrans.46.581.
[29] C. Lerchbacher, S. Zinner, H. Leitner, Retained Austenite Decomposition and Carbide Formation During Tempering a Hot-Work Tool Steel X38CrMoV5-1 Studied by Dilatometry and Atom Probe Tomography, Metall. Mater. Trans. A. 43 (2012) 4989–4998. doi:10.1007/s11661-012-1358-3.
[30] L. Thijs, F. Verhaeghe, T. Craeghs, J.V. Humbeeck, J.-P. Kruth, A study of the microstructural evolution during selective laser melting of Ti–6Al–4V, Acta Mater. 58 (2010) 3303–3312. doi:10.1016/j.actamat.2010.02.004.
[31] A. Fedrizzi, Production of steel matrix composites by mechanical milling and spark plasma sintering, phd, University of Trento, 2013. http://eprints-phd.biblio.unitn.it/1025/ (accessed April 17, 2016).
[32] X. He, G. Yu, J. Mazumder, Temperature and composition profile during double-track laser cladding of H13 tool steel, J. Phys. Appl. Phys. 43 (2010) 015502. doi:10.1088/0022-3727/43/1/015502.
[33] F. Deirmina, M. Pellizzari, Strengthening mechanisms in an ultrafine grained powder metallurgical hot work tool steel produced by high energy mechanical milling and spark plasma sintering, Mater. Sci. Eng. A. 743 (2019) 349–360. doi:10.1016/j.msea.2018.11.093.
[34] F. Deirmina, M. Pellizzari, M. Federici, Production of a Powder Metallurgical Hot Work Tool Steel with Harmonic Structure by Mechanical Milling and Spark Plasma Sintering, Metall. Mater. Trans. A. 48 (2017) 1910–1920. doi:10.1007/s11661-017-3957-5.
[35] M. Pellizzari, A. Fedrizzi, M. Zadra, Spark Plasma Co-Sintering of Mechanically Milled Tool Steel and High Speed Steel Powders, Materials. 9 (2016) 482. doi:10.3390/ma9060482.
[36] A. Hohenwarter, R. Pippan, Fracture of ECAP-deformed iron and the role of extrinsic toughening mechanisms, Acta Mater. 61 (2013) 2973–2983. doi:10.1016/j.actamat.2013.01.057.
[37] K.-H. Schwalbe, On the influence of microstructure on crack propagation mechanisms and fracture toughness of metallic materials, Eng. Fract. Mech. 9 (1977) 795–832. doi:10.1016/0013-7944(77)90004-2.
[38] K. Nakazawa, G. Krauss, Microstructure and fracture of 52100 steel, Metall. Trans. A. 9 (1978) 681–689. doi:10.1007/BF02659925.